Original Article

Differentiating mass-forming intrahepatic cholangiocarcinoma from atypical hepatocellular carcinoma using Gd-EOB-DTPA-enhanced magnetic resonance imaging combined with serum markers in at-risk patients with hepatitis B virus

Dingsheng Han[1]^, Yalin Li[1]^, Xu He[1]^, Jiacheng Zhang[1]^, Yanru Zhou[2,3]^, Jiajia Zhang[4]^, Lan Zhang[2,3]^

[1]Imaging and Nuclear Medicine Department, Henan University of Chinese Medicine, Zhengzhou, China; [2]Department of MRI, the First Affiliated Hospital of Henan University of Chinese Medicine, Zhengzhou, China; [3]Zhengzhou Key Laboratory of Intelligent Analysis and Utilization of Traditional Chinese Medicine Information, Henan University of Chinese Medicine, Zhengzhou, China; [4]Department of Radiology, Gold Coast University Hospital, School of Medicine, Bond University, Gold Coast, Queensland, Australia

Contributions: (I) Conception and design: D Han, L Zhang; (II) Administrative support: Jiajia Zhang, L Zhang; (III) Provision of study materials or patients: D Han, X He, Jiacheng Zhang; (IV) Collection and assembly of data: D Han, Jiacheng Zhang; (V) Data analysis and interpretation: D Han, X He; (VI) Manuscript writing: All authors; (VII) Final approval of manuscript: All authors.

Correspondence to: Lan Zhang, MD. Department of MRI, the First Affiliated Hospital of Henan University of Chinese Medicine, No. 19 Renmin Road, Zhengzhou 450000, China; Zhengzhou Key Laboratory of Intelligent Analysis and Utilization of Traditional Chinese Medicine Information, Henan University of Chinese Medicine, No. 156 Jinshui East Road, Zhengzhou 450046, China. Email: 13837187787@163.com.

Background: The precise differentiation of intrahepatic cholangiocarcinoma (ICC) from atypical hepatocellular carcinoma (HCC) is vital for treatment strategy and prognostic prediction. In clinical practice, nearly 40% of HCCs demonstrate atypical manifestations, particularly HCCs with rim arterial phase hyperenhancement (APHE), which is challenging to differentiate from mass-forming ICC. Thus, we aimed to develop a diagnostic regimen of gadolinium ethoxybenzyl diethylenetriamine pentaacetic acid (Gd-EOB-DTPA) contrast-enhanced magnetic resonance imaging (MRI) combined with serum tumor markers in differentiating mass-forming ICC from atypical HCC in at-risk patients with the hepatitis B virus (HBV).

Methods: This study enrolled 129 patients with pathologically proven mass-forming ICCs (n=53) and atypical HCCs (n=76) who had undergone preoperative Gd-EOB-DTPA contrast-enhanced MRI. The clinical data and imaging findings were analyzed. Univariate and multivariate logistic analyses were performed to identify the independent predictors for differentiating mass-forming ICCs from atypical HCCs. The diagnostic performance was evaluated using receiver operating characteristic (ROC) curves, and DeLong test was used to compare the areas under curves of all independent predictors.

Results: Univariate logistic regression analysis revealed normal alpha fetoprotein (AFP), elevated carbohydrate antigen 19-9 (CA19-9) level, elevated carcinoma embryonic antigen (CEA) level, central hyperintensity on T2-weighted imaging (T2WI), central hypointensity on T2WI, and targetoid sign on hepatobiliary phase (HBP) and targetoid restriction on diffusion-weighted imaging (DWI) were more likely to be significant predictors favoring mass-forming ICCs (all P values <0.05). In contrast, multifocal hyperintensity on T2WI and capsule sign were more frequently seen in patients with atypical HCC (all P values <0.05). Multivariate analysis revealed normal AFP, elevated CA19-9 level, targetoid sign on HBP, and targetoid restriction on DWI (all P=0.001) were independent predictors for differentiating mass-forming

^ ORCID: Dingsheng Han, 0000-0001-9538-2416; Yalin Li, 0009-0007-7622-7454; Xu He, 0009-0009-1700-4001; Jiacheng Zhang, 0009-0008-4164-2321; Yanru Zhou, 0000-0002-1311-4184; Jiajia Zhang, 0000-0002-7615-2137; Lan Zhang, 0000-0002-7891-3964.

ICCs from atypical HCCs; DeLong test showed that the area under curve (AUC) increased to 0.949 when the above predictors were combined (all P values <0.05), and the sensitivity, specificity, and accuracy of the combined independent predictors were 88.7%, 93.4%, and 91.5%, respectively.

Conclusions: A diagnostic regimen integrating tumor markers (AFP, CA19-9) and imaging biomarkers (targetoid restriction on DWI and/or targetoid sign on HBP) using Gd-EOB-DTPA-enhanced MRI could help to differentiate mass-forming ICCs from atypical HCCs and achieve high diagnostic performance of mass-forming ICCs in at-risk patients with the HBV.

Keywords: Mass-forming intrahepatic cholangiocarcinoma (mass-forming ICC); atypical hepatocellular carcinoma (atypical HCC); magnetic resonance imaging (MRI); gadolinium ethoxybenzyl diethylenetriamine pentaacetic acid (Gd-EOB-DTPA); hepatobiliary phase (HBP)

Submitted Mar 26, 2023. Accepted for publication Aug 24, 2023. Published online Sep 05, 2023.
doi: 10.21037/qims-23-396
View this article at: https://dx.doi.org/10.21037/qims-23-396

Introduction

Chronic hepatitis virus infection is the main etiology of primary liver cancer (PLC), and 80–90% of PLCs occur in patients with hepatitis B virus (HBV)-related cirrhosis (1,2). Hepatocellular carcinoma (HCC) and intrahepatic cholangiocarcinoma (ICC) are the 2 most common types of PLC, with the incidence of ICC increasing in recent years (1). It is crucial to differentiate mass-forming ICC from HCC in clinical practice because their treatment and prognosis are significantly different. In Asian countries, transcatheter arterial chemoembolization (TACE), radiofrequency ablation (RFA), and other locoregional therapies are frequently recommended for HCC. In contrast, surgery remains the first choice for resectable mass-forming ICCs, and the prognosis of mass-forming ICCs is poor, with a 5-year survival rate of just 5–10% (3-5). Therefore, the early and precise differentiation between mass-forming ICC and HCC is important for optimal therapeutic planning and prognostic prediction.

The Liver Imaging Reporting and Data System (LI-RADS) is a comprehensive system devised to standardize the interpretation and reporting of computed tomography (CT) and magnetic resonance imaging (MRI) in patients at risk for HCC (6). LI-RADS M (LR-M) is a special category of LI-RADS, which refers to likely or definitely malignant tumors that are not specific to HCC (7). Atypical HCC and ICC account for approximately 36% and 30% of LR-M lesions, respectively. However, there is an overlap in both clinical and imaging features, which makes the differentiation between atypical HCC and mass-forming ICC highly challenging (8-12). In addition, serum tumor markers, such as alpha fetoprotein (AFP), carbohydrate antigen 19-9 (CA19-9) and carcinoma embryonic antigen (CEA) play an important role in the diagnosis and surveillance of LR-M lesions. Clinically, serum tumor markers are easily available and much less costly than is imaging, but their sensitivity and specificity are comparatively low (8,13).

Gadolinium ethoxybenzyl diethylenetriamine pentaacetic acid (Gd-EOB-DTPA) is a hybrid MRI contrast agent that combines the properties of hepatocyte specificity and extracellular contrast agents. In the hepatobiliary phase (HBP), it can facilitate the delineation of focal hepatic lesions and provide more detailed information for the detection and characterization of lesions (14). Gd-EOB-DTPA contrast-enhanced MRI has been recommended for HCC diagnosis by the guidelines of organizations from various Asian countries, including the Asian Pacific Association for the Study of the Liver (APASL), the Korean Liver Cancer Study Group and the National Cancer Center (KLCSG-NCC), Japan Society of Hepatology (JSH), and Standardization for Diagnosis and Treatment of Hepatocellular Carcinoma of China (15).

The aim of our study was to evaluate the combined utility of imaging features on Gd-EOB-DTPA contrast-enhanced MRI with serum tumor markers in the differential diagnosis of mass-forming ICC from atypical HCC in at-risk patients with HBV infection.

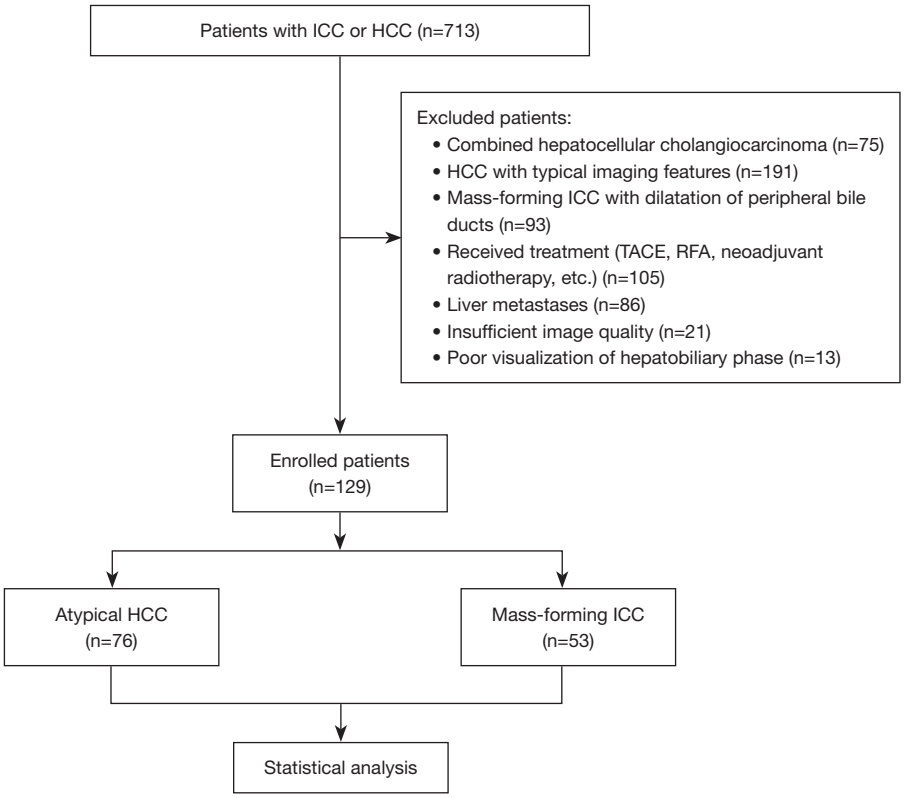

Figure 1 Flowchart of sample collection. ICC, intrahepatic cholangiocarcinoma; HCC, hepatocellular carcinoma; TACE, transcatheter arterial chemoembolization; RFA, radiofrequency ablation.

Methods

Patients

This single-center retrospective cohort study was conducted in accordance with the Declaration of Helsinki (as revised in 2013) and was approved by the Institutional Review Board of the First Affiliated Hospital of Henan University of Chinese Medicine (No. 2023HL-034-01). Written informed consent was waived due to the retrospective nature of the study. From September 2019 to July 2022, consecutive patients who underwent Gd-EOB-DTPA contrast-enhanced MRI prior to surgery were retrospectively enrolled at our hospital. The inclusion criteria were the following: (I) with chronic hepatitis B and/or hepatitis B cirrhosis; (II) pathologically proven mass-forming ICC categorized as LR-M; (III) pathologically proven atypical HCC with imaging features of rim arterial phase hyperenhancement (APHE) categorized as LR-M (16); (IV) with no dilatation of the peripheral bile ducts (17); and (V) no history of prior treatment (TACE, RFA, neoadjuvant radiotherapy, etc.). Meanwhile, the exclusion criteria were the following: (I) classical HCC with typical APHE followed by subsequent washout on the portal venous phase (PVP) according to LI-RADS; (II) surgically proven combined hepatocellular-cholangiocarcinoma (cHCC-CCA); (III) hepatic metastases or a history of extrahepatic malignancies; (IV) insufficient image quality with severe artifacts; and (V) poor visualization of the HBP owing to liver dysfunction or biliary obstruction. A total of 129 consecutive patients' demographic, clinical, and laboratory data were included (*Figure 1*). In 53 of these patients, pathologically proven mass-forming ICCs were identified. As the control group, 76 patients with pathologically proven HCCs who did not exhibit a typical enhancement pattern were selected. The selection of atypical HCCs was based on a consensus of 3 radiologists in consideration of the inclusion and exclusion criteria.

Image acquisition

Magnetic resonance (MR) images were acquired with a 3.0T MR imaging system (Ingenia CX, Philips, Amsterdam,

Table 1 MRI scanning parameters

Sequences	TR (ms)	TE (ms)	FOV (mm^2)	Slice thickness (mm)	Slice gap (mm)	Matrix
T1WI	10	2.3	400×384	6	1	268×176
DCE-T1WI	3.1	1.06	400×384	5	1	180×200
FS-T2WI	582	80	400×384	6	1	276×251
DWI	764	65	400×384	6	1	132×114
HBP	3.2	1.1	400×384	5	1	200×200

MRI, magnetic resonance imaging; TR, repetition time; TE, time to echo; FOV, field of view; T1WI, T1-weighted imaging; DCE, dynamic contrast-enhanced; FS, fat-suppression; T2WI, T2-weighted imaging; DWI, diffusion-weighted imaging; HBP, hepatobiliary phase.

The Netherlands) equipped with a 16-channel body phased-array coil. The routine MR sequences were as follows: (I) modified Dixon in phase and out of phase T1-weighted imaging (T1WI); (II) dynamic contrast-enhanced T1WI (DCE-T1WI) obtained using modified Dixon-fast field echo and performed after intravenous injection of 0.1 mL/kg of Gd-EOB-DTPA (Xian Ai, Chia Tai Tianqing Pharmaceutical Co. Ltd., Hangzhou, China) at a rate of 1 mL/s and followed by a 15-mL saline flush with the same speed using bolus-tracking methods and with the early and late arterial phases, PVP, and transitional phase (TP) being acquired at 15–20, 60, and 120 s from the start of Gd-EOB-DTPA, respectively; (III) T2-weighted imaging (T2WI) with fat suppression (FS); (IV) diffusion-weighted imaging (DWI) performed using single-shot echo planar imaging (b values were 50 and 800 s/mm^2); and (V) HBP acquired at 15–20 min after the administration of Gd-EOB-DTPA (*Table 1*).

Imaging analysis

Three abdominal radiologists (with 10, 15, and 20 years of experience, respectively) who were blinded to the patients' data evaluated MRI images independently, with any discrepancies being resolved through discussion and consensus. The imaging features evaluated were as follows: (I) location (left lobe, right lobe, and caudate lobe), shape (irregular, lobulated, and globular), and maximum diameter; (II) central hyperintensity on T2WI (markedly higher than the signal intensity of tumor periphery), central hypointensity on T2WI (darker than the signal intensity of the hepatic parenchyma), and multifocal hyperintensity on T2WI (3 or more tiny hyperintense foci); (III) capsule sign (peripheral enhancing rim around the tumor on PVP or TP); (IV) nodule in nodule; (V) mosaic appearance; (VI) rim APHE; (VII) peripheral enhancement or peripheral washout on PVP; (VIII) targetoid sign on HBP (concentric enhancement with moderate to marked hypointensity in the periphery and mild hypointensity in the center); and (IX) targetoid restriction on DWI (concentric pattern characterized by restricted diffusion in the periphery with less or no restricted diffusion in the center) (18-20). The signal intensity of lesions was classified as hyperintensity, isointensity, and hypointensity, with the surrounding normal liver parenchyma being used as a reference in each MRI sequence.

Statistical analysis

Continuous variables are expressed as the mean ± standard deviation ($\overline{x} \pm s$) for normal distributions and as the median (interquartile range) for a nonnormal distributions, with their statistical differences being analyzed with Student *t*-test or Mann-Whitney test. Categorical variables are described as numbers of cases, and percentages and were compared using the χ^2 test or Fisher exact tests. The statistically significant variables obtained from univariate logistic regression were used to conduct multivariate logistic regression to determine the most independent predictors for differentiating mass-forming ICC from atypical HCC. The diagnostic performance of each predictor and its combination were evaluated using the receiver operating characteristic (ROC) curves, and the area under curve (AUC), sensitivity, specificity, accuracy, positive predictive value (PPV), and negative predictive value (NPV) were calculated. The DeLong test was used to compare the AUCs of all independent predictors. All statistical analyses were conducted using SPSS (version 26.0, IBM Corp., Armonk, NY, USA) or MedCalc (MedCalc Software, Ostend, Belgium) software. A P value of

Table 2 Comparison of clinicopathological characteristics between mass-forming ICC and atypical HCC

Clinical parameters	Mass-forming ICC (n=53)	Atypical HCC (n=76)	χ^2/t	P value
Age (years)	60.96±8.04	57.67±11.65	1.898	0.060
Sex			0.674	0.412
Male	43 (81.1)	57 (75.0)		
Female	10 (18.9)	19 (25.0)		
Child-Pugh scores			1.422	0.233
Grade A	41 (77.4)	65 (85.5)		
Grade B	12 (22.6)	11 (14.5)		
AFP (ng/mL)			19.631	<0.001
≤7.0	37 (69.8)	23 (30.3)		
>7.0	16 (30.2)	53 (69.7)		
CA19-9 (U/mL)			44.347	<0.001
≤37	12 (22.6)	62 (81.6)		
>37	41 (77.4)	14 (18.4)		
CEA (ng/mL)			6.752	0.009
≤5	36 (67.9)	66 (86.8)		
>5	17 (32.1)	10 (13.2)		

Data are number of patients (percentage) or mean ± standard deviation. The age comparisons were performed using the independent samples *t*-test. Except where noted, data were compared using the χ^2 test. ICC, intrahepatic cholangiocarcinoma; HCC, hepatocellular carcinoma; AFP, alpha fetoprotein; CA19-9, carbohydrate antigen 19-9; CEA, carcinoma embryonic antigen.

<0.05 was considered statistically significant.

Results

Patient clinical characteristics

A total of 129 patients were enrolled, including 53 with mass-forming ICC (43 males and 10 females; mean age 60.96±8.04 years) and 76 with atypical HCC (57 males and 19 females; mean age 57.67±11.65 years). Elevated CA19-9 and CEA were found in the mass-forming ICC group, while elevated AFP was found in the atypical HCC group (all P values <0.05). No significant differences were found in sex, age, or Child-Pugh scores between the 2 groups (all P values <0.05). Among the MRI features, central hyperintensity on T2WI, central hypointensity on T2WI, targetoid sign on HBP, and targetoid restriction on DWI were significant imaging findings associated with mass-forming ICC, while multifocal hyperintensity on T2WI and capsule sign were associated with atypical HCC (all P values <0.05). No other variables were significantly different between the 2 groups (all P values ≥0.05). The clinical and imaging characteristics are described in *Tables 2,3* and *Figures 2-6*.

Univariate logistic regression analysis revealed that normal AFP, elevated CA19-9, elevated CEA, central hyperintensity on T2WI, central hypointensity on T2WI, targetoid sign on HBP, and targetoid restriction on DWI were more likely to be significant predictors of mass-forming ICC (all P values <0.05). In contrast, multifocal hyperintensity on T2WI and capsule sign were more frequently observed in atypical HCC (all P values <0.05). Multivariate logistic regression analysis indicated that normal AFP [odds ratio (OR), 4.224; 95% confidence interval (CI): 1.050–16.994; P=0.042], elevated CA19-9 (OR, 7.086; 95% CI: 1.765–28.442; P=0.006), targetoid sign on HBP (OR, 9.913; 95% CI: 2.141–45.906; P=0.003), and targetoid restriction on DWI (OR, 12.202; 95% CI: 2.750–54.152; P=0.001) were independent predictors for differentiating mass-forming ICC from atypical HCC. The results of univariate and multivariate analysis of variables are shown in *Table 4*.

Table 3 Comparison of MRI features between mass-forming ICC and atypical HCC

Variables	Mass-forming ICC (n=53)	Atypical HCC (n=76)	χ^2/t	P value
Shape			1.772	0.412
Irregular	32 (60.4)	37 (48.7)		
Lobulated	9 (17.0)	18 (23.7)		
Globular	12 (22.6)	21 (27.6)		
Location				
Right liver lobe	36 (67.9)	54 (71.1)	0.439	0.803
Left liver lobe	11 (20.8)	16 (21.1)		
Caudate lobe	6 (11.3)	6 (7.9)		
Maximum diameter (mm)	29.1±5.7	31.1±5.9	1.932	0.056
Central hyperintensity on T2WI	21 (39.6)	17 (22.4)	4.473	0.034
Central hypointensity on T2WI	36 (67.9)	34 (44.7)	6.765	0.009
Multifocal hyperintensity on T2WI	5 (9.4)	20 (26.3)	5.696	0.017
Nodule in nodule	6 (11.3)	11 (14.5)	0.271	0.602
Mosaic sign	11 (20.8)	21 (27.6)	0.792	0.374
Rim APHE	27 (50.9)	31 (40.8)	1.301	0.254
Peripheral washout	6 (11.3)	8 (10.5)	0.020	0.887
Peripheral enhancement	41 (77.4)	62 (81.6)	0.346	0.557
Capsule sign	3 (5.7)	22 (28.9)	10.838	0.001
Targetoid sign	46 (86.8)	8 (10.5)		
Targetoid sign on HBP	40 (75.5)	7 (9.2)	59.195	<0.001
Targetoid restriction on DWI	44 (83.0)	8 (10.5)	68.198	<0.001

Data are number of patients (percentage) or mean ± standard deviation. The maximum diameter comparisons were performed using the independent samples *t*-test. Except where noted, data were compared using the χ^2 test. MRI, magnetic resonance imaging; ICC, intrahepatic cholangiocarcinoma; HCC, hepatocellular carcinoma; T2WI, T2-weighted imaging; APHE, arterial phase hyperenhancement; HBP, hepatobiliary phase; DWI, diffusion-weighted imaging.

The ROC curve showed that the AUCs for predicting mass-forming ICC of normal AFP, elevated CA19-9, targetoid sign on HBP, and targetoid restriction on DWI were 0.698, 0.795, 0.831, and 0.862, respectively (*Figure 7*); the DeLong test showed that when the above independent predictors were combined, the AUC increased to 0.949 (Z=6.158, Z=4.489, Z=3.851, Z=3.336; all P values <0.05). In addition, the sensitivity, specificity, accuracy, PPV, and NPV of the combination of independent predictors were 88.7%, 93.4%, 91.5%, 90.4%, and 88.8%, respectively, representing a significant improvement in the diagnostic performance for mass-forming ICC. The results of the diagnostic performance are described in *Table 5*.

Discussion

According to the World Health Organization (WHO), HBV is the most common cause of liver cirrhosis worldwide, with approximately 296 million people with HBV. The incidence of PLC developing in patients with HBV cirrhosis may be up to 30 times greater than that developing in patients with non-HBV cirrhosis (21,22). Therefore, HBV cirrhosis has been recognized as an important risk factor for the development of PLC. The 2 most common types of PLC, ICC and HCC, can be found in patients with chronic hepatitis B and/or HBV cirrhosis, but the treatment for each is vastly different (5). Accurate

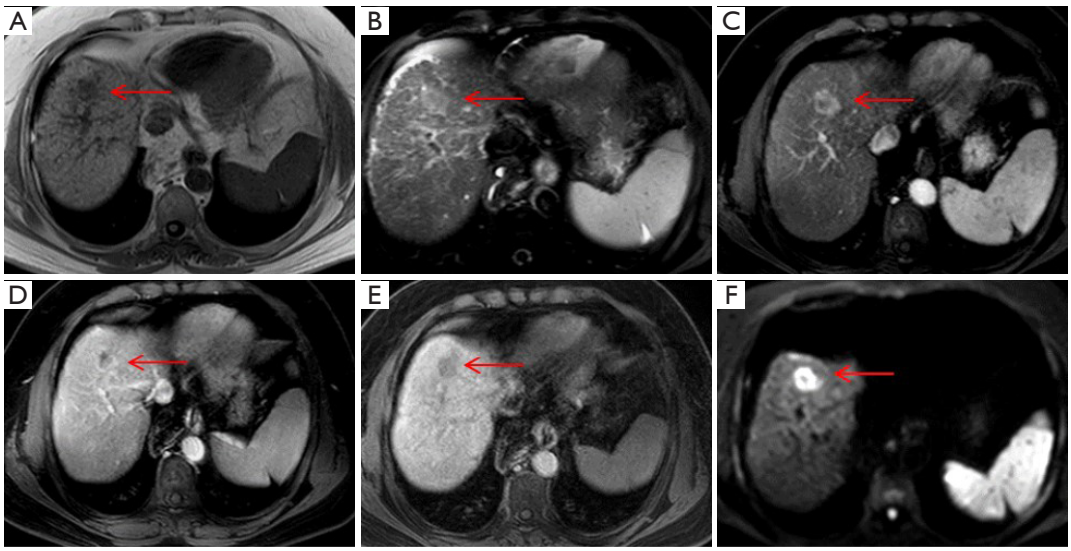

Figure 2 A histopathologically proven mass-forming ICC in a 65-year-old man with hepatitis B cirrhosis. The patient's AFP and CA19-9 levels were 4.2 ng/mL and 48 IU/mL, respectively. On Gd-EOB-DTPA contrast-enhanced MRI, there was a 14-mm tumor (arrow) in segment VIII, with hypointensity on T1WI (A) and hyperintensity on T2WI (B), rim APHE (C), peripheral washout on PVP (D), hypointensity on HBP (E), and targetoid restriction on DWI (F). ICC, intrahepatic cholangiocarcinoma; AFP, alpha fetoprotein; CA19-9, carbohydrate antigen 19-9; Gd-EOB-DTPA, gadolinium ethoxybenzyl diethylenetriamine pentaacetic acid; MRI, magnetic resonance imaging; T1WI, T1-weighted imaging; T2WI, T2-weighted imaging; APHE, arterial phase hyperenhancement; PVP, portal venous phase; HBP, hepatobiliary phase; DWI, diffusion-weighted imaging.

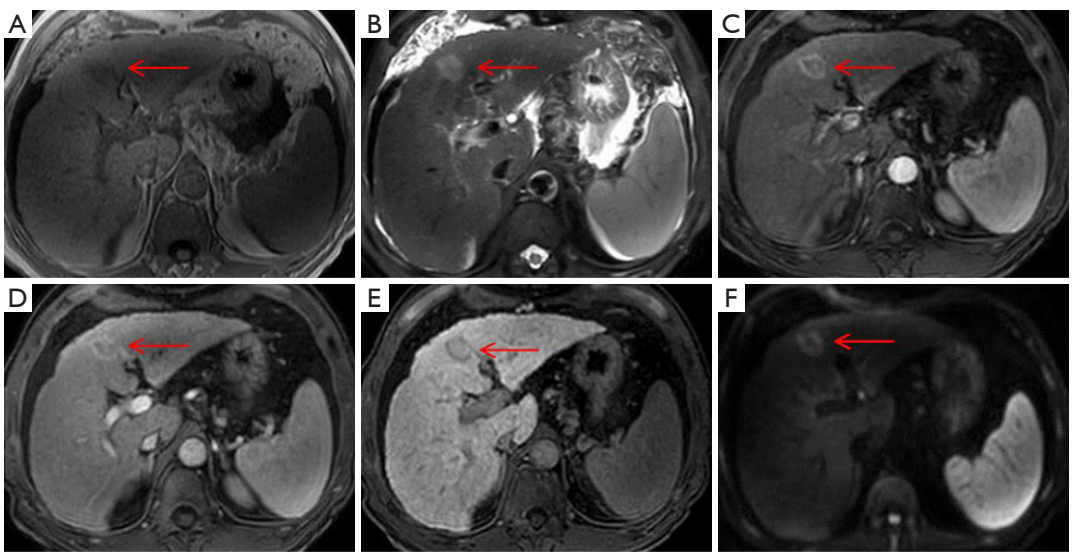

Figure 3 A histopathologically proven mass-forming ICC in a 61-year-old man with chronic hepatitis B. The patient's AFP and CA19-9 levels were 6.1 ng/mL and 57 IU/mL, respectively. On Gd-EOB-DTPA contrast-enhanced MRI, there was a 24-mm tumor (arrow) in segment IV, which showed hypointensity on T1WI (A) and hyperintensity on T2WI (B), rim APHE (C), peripheral enhancement on PVP (D), targetoid sign on HBP (E), and targetoid restriction on DWI (F). ICC, intrahepatic cholangiocarcinoma; AFP, alpha fetoprotein; CA19-9, carbohydrate antigen 19-9; Gd-EOB-DTPA, gadolinium ethoxybenzyl diethylenetriamine pentaacetic acid; MRI, magnetic resonance imaging; T1WI, T1-weighted imaging; T2WI, T2-weighted imaging; APHE, arterial phase hyperenhancement; PVP, portal venous phase; HBP, hepatobiliary phase; DWI, diffusion-weighted imaging.

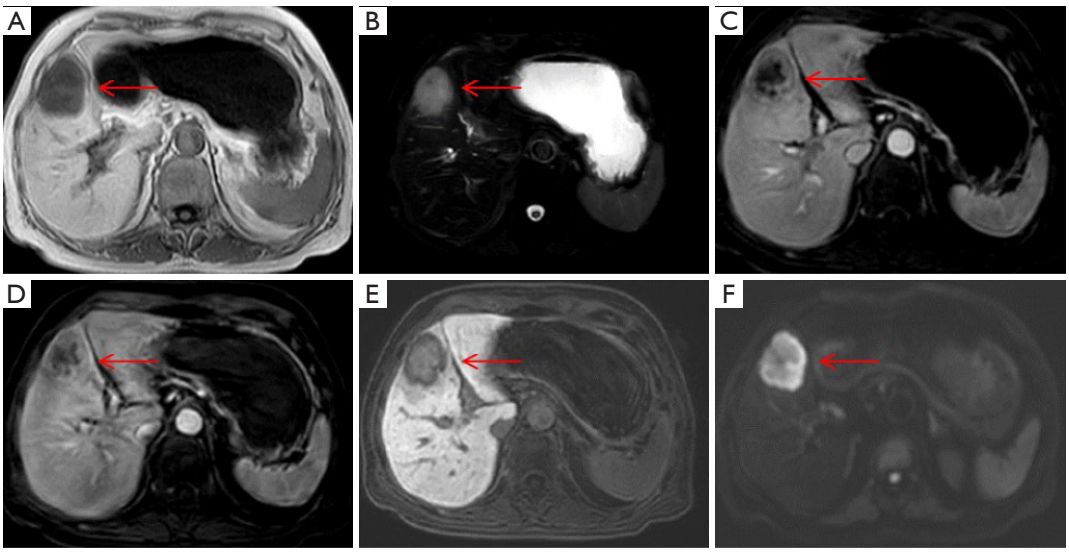

Figure 4 A histopathologically proven mass-forming ICC in a 70-year-old man with chronic hepatitis B. The patient's AFP and CA19-9 levels were 2.4 ng/mL and 153 IU/mL, respectively. On Gd-EOB-DTPA contrast-enhanced MRI, there was a 41-mm tumor (arrow) in segment IV, with hypointensity on T1WI (A) and hyperintensity on T2WI (B), rim APHE (C), peripheral enhancement (D), targetoid sign on HBP (E), and targetoid restriction on DWI (F). ICC, intrahepatic cholangiocarcinoma; AFP, alpha fetoprotein; CA19-9, carbohydrate antigen 19-9; Gd-EOB-DTPA, gadolinium ethoxybenzyl diethylenetriamine pentaacetic acid; MRI, magnetic resonance imaging; T1WI, T1-weighted imaging; T2WI, T2-weighted imaging; APHE, arterial phase hyperenhancement; HBP, hepatobiliary phase; DWI, diffusion-weighted imaging.

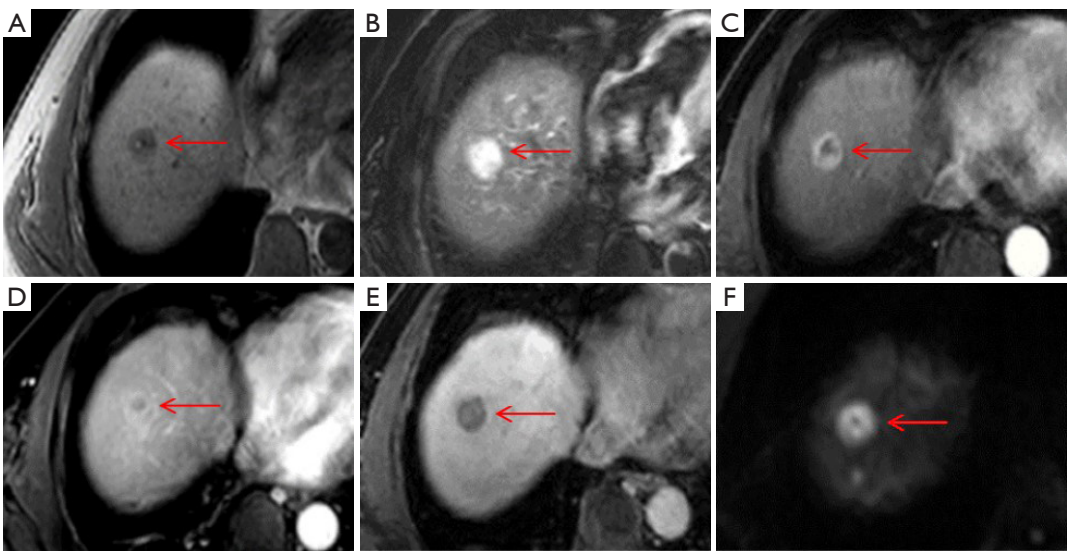

Figure 5 A histopathologically proven scirrhous HCC in a 61-year-old man with chronic hepatitis B. The patient's AFP and CA19-9 levels were 75.3 ng/mL and 18 IU/mL, respectively. On Gd-EOB-DTPA contrast-enhanced MRI, there was a 15-mm tumor (arrow) in segment VIII, with hypointensity on T1WI (A) and hyperintensity on T2WI (B), rim APHE (C), peripheral enhancement on PVP (D), targetoid sign on HBP (E), and targetoid restriction on DWI (F). HCC, hepatocellular carcinoma; AFP, alpha fetoprotein; CA19-9, carbohydrate antigen 19-9; Gd-EOB-DTPA, gadolinium ethoxybenzyl diethylenetriamine pentaacetic acid; MRI, magnetic resonance imaging; T1WI, T1-weighted imaging; T2WI, T2-weighted imaging; APHE, arterial phase hyperenhancement; PVP, portal venous phase; HBP, hepatobiliary phase; DWI, diffusion-weighted imaging.

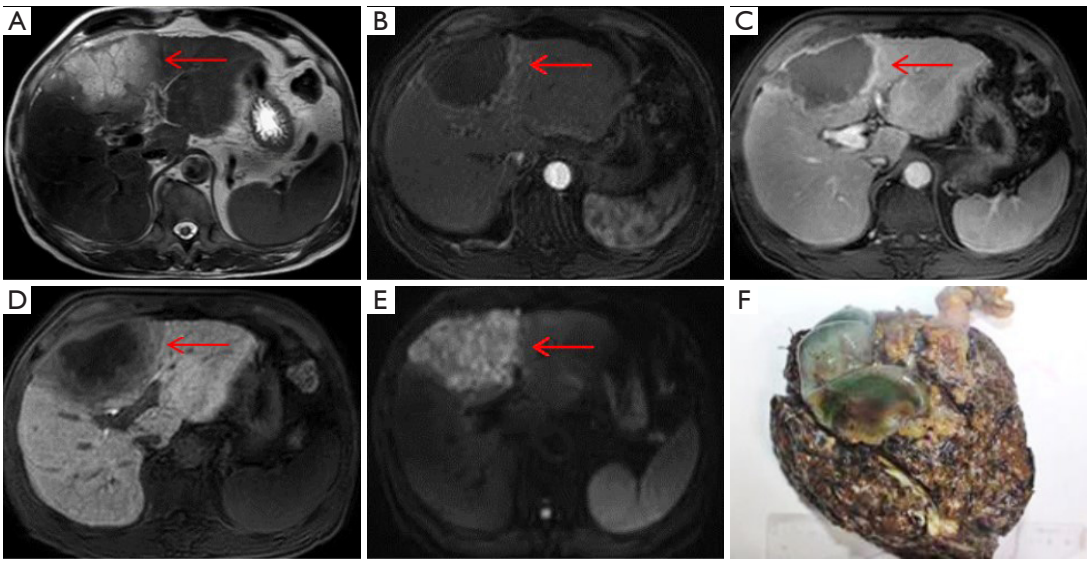

Figure 6 A histopathologically proven sarcomatous HCC in a 66-year-old man with hepatitis B cirrhosis. The patient's AFP and CA19-9 levels were 83.6 ng/mL and 23 IU/mL, respectively. On Gd-EOB-DTPA contrast-enhanced MRI, there was a 100-mm tumor (arrow) in the right anterior lobe the liver with multifocal hyperintensity on T2WI (A), rim APHE (B), peripheral enhancement on PVP (C), hypointensity on HBP (D), and multifocal hyperintensity on DWI (E). Gross specimen of sarcomatous HCC (F). HCC, hepatocellular carcinoma; AFP, alpha fetoprotein; CA19-9, carbohydrate antigen 19-9; Gd-EOB-DTPA, gadolinium ethoxybenzyl diethylenetriamine pentaacetic acid; MRI, magnetic resonance imaging; T2WI, T2-weighted imaging; APHE, arterial phase hyperenhancement; PVP, portal venous phase; HBP, hepatobiliary phase; DWI, diffusion-weighted imaging.

differentiation between HCC and ICC is thus essential for adequate treatment planning, and integration of imaging features and tumor biomarkers to distinguish ICC from HCC is warranted. Although the imaging diagnosis of HCC is mainly based on the typical enhancement patterns of non-rim APHE and nonperipheral washout according to LI-RADS, nearly 40% of HCCs demonstrate atypical clinical manifestations, particularly HCCs with rim APHE, which is challenging to differentiate from mass-forming ICC (23,24). Although serum tumor markers CA19-9 and AFP have been shown to have some differential diagnostic capacity, their diagnostic sensitivity is comparatively low since some patients do not express these markers (5,15). Gd-EOB-DTPA is a liver-specific MRI contrast agent that can provide both multiparametric DCE and hepatobiliary imaging (14). Gd-EOB-DTPA contrast-enhanced MRI combined with a DWI sequence can be helpful for distinguishing mass-forming ICC from atypical HCC.

Univariate analysis demonstrated that multifocal hyperintensity on T2WI (26.3%) and capsule sign (28.9%) were important imaging findings suggestive of atypical HCC. The presence of multifocal hyperintensity on T2WI could be attributed to the internal fibrotic septum and hemorrhage and necrosis within the tumor (25). As shown in a representative case of sarcomatous HCC (*Figure 6A*), necrosis could be responsible for the multifocal hyperintensity on T2WI. Capsule sign is usually caused by the compression of the surrounding liver tissues owing to the expansive growth of the tumor (25). Univariate analysis also revealed that central hyperintensity on T2WI (39.6%) and central hypointensity on T2WI (67.9%) were more often seen with mass-forming ICC. The signal intensity of mass-forming ICC on T2WI is closely related to the density of the central fibrous area, the degree of necrosis, inflammation, and edema within the tumor (26,27). The presence of central hypointensity on T2WI could reflect fibrosis in the central areas and tends to be a characteristic imaging feature of ICC. Some mass-forming ICCs that display hyperintense areas on T2WI are found to have liquefactive necrosis in the tumors in histological findings (27).

It is well known the typical enhancement pattern of mass-forming ICC manifests as initial rim enhancement on the arterial phase, followed by progressive and concentric fill-in during DCE imaging (within 5–7 min) with

Table 4 Univariate and multivariate analysis of variables for differentiating mass-forming ICC from atypical HCC

Variables	Univariate analysis		Multivariate analysis	
	OR (95% CI)	P value	OR (95% CI)	P value
Age (years)	1.032 (0.996–1.069)	0.080	–	–
Sex (male/female)	0.698 (0.295–1.652)	0.413	–	–
Child-Pugh grade (A/B)	0.578 (0.234–1.432)	0.236	–	–
Normal AFP	5.329 (2.483–11.438)	<0.001	4.224 (1.050–16.994)	0.042
Elevated CA19-9	15.131 (6.364–35.976)	<0.001	7.086 (1.765–28.442)	0.006
Elevated CEA	3.117 (1.292–7.517)	0.011	1.701 (0.326–8.871)	0.529
Shape				
Irregular	1.606 (0.789–3.270)	0.191	–	–
Lobulated	0.659 (0.270–1.606)	0.359	–	–
Globular†	–	–	–	–
Location				
Right liver lobe	0.863 (0.403–1.846)	0.704	–	–
Left liver lobe	0.982 (0.414–2.328)	0.967	–	–
Caudate lobe†	–	–	–	–
Maximum diameter	0.942 (0.886–1.002)	0.058	–	–
Central hyperintensity on T2WI	2.278 (1.054–4.923)	0.036	2.623 (0.440–15.653)	0.290
Central hypointensity on T2WI	2.616 (1.257–5.444)	0.010	3.150 (0.499–19.895)	0.222
Multifocal hyperintensity on T2WI	0.292 (0.102–0.836)	0.022	0.395 (0.036–4.371)	0.449
Nodule in nodule	0.754 (0.261–2.184)	0.603	–	–
Mosaic sign	0.686 (0.298–1.577)	0.375	–	–
Rim APHE	1.507 (0.744–3.056)	0.255	–	–
Peripheral washout	1.085 (0.353–3.332)	0.887	–	–
Peripheral enhancement	0.772 (0.324–1.834)	0.557	–	–
Capsule sign	0.147 (0.042–0.522)	0.003	0.275 (0.027–2.780)	0.274
Targetoid sign				
Targetoid sign on HBP	30.330 (11.180–82.279)	<0.001	9.913 (2.141–45.906)	0.003
Targetoid restriction on DWI	41.556 (14.909–115.830)	<0.001	12.202 (2.750–54.152)	0.001

†, data were used as a reference variable. ICC, intrahepatic cholangiocarcinoma; HCC, hepatocellular carcinoma; OR, odds ratio; CI, confidence interval; AFP, alpha fetoprotein; CA19-9, carbohydrate antigen 19-9; CEA, carcinoma embryonic antigen; T2WI, T2-weighted imaging; APHE, arterial phase hyperenhancement; HBP, hepatobiliary phase; DWI, diffusion-weighted imaging.

gadopentetate dimeglumine (12). However, rim APHE is not a characteristic imaging feature of mass-forming ICCs, whereas some atypical HCCs, such as scirrhous HCCs (*Figure 5C*), sarcomatous HCCs (*Figure 6C*), and small HCCs without full arterial hypervascularization may show ring-like enhancement on the arterial phase (23,24). Moreover, the presence of a peripheral enhancing rim on the PVP is another common finding of ICCs, while scirrhous HCCs or sarcomatous HCCs can also demonstrate persistent rim enhancement on the PVP (28). Nevertheless, multivariate analysis demonstrated that targetoid appearance on DWI and/or HBP, elevated CA19-

9, and normal AFP were significant independent predictors of mass-forming ICC, as 46 cases of ICC (86.8%) showed targetoid appearance, including 44 (83.0%) with targetoid sign on HBP and 40 (75.5%) with targetoid restriction on DWI. As reported in previous studies by Min *et al.* (29), targetoid appearance on DWI and/or HBP was present in 87.3% of mass-forming ICCs, whereas only 15.7% of HCCs had a targetoid sign. In a study conducted by Choi *et al.* (30), the occurrence of targetoid sign on HBP and targetoid restriction on DWI were 86.7% and 90.8% among patients with ICC, respectively, and targetoid appearance both on HBP and DWI were shown to be significant characteristic for the imaging diagnosis of mass-forming ICC. In clinical practice, the co-occurrence of targetoid appearance on HBP and DWI can improve the diagnostic confidence for mass-forming ICC.

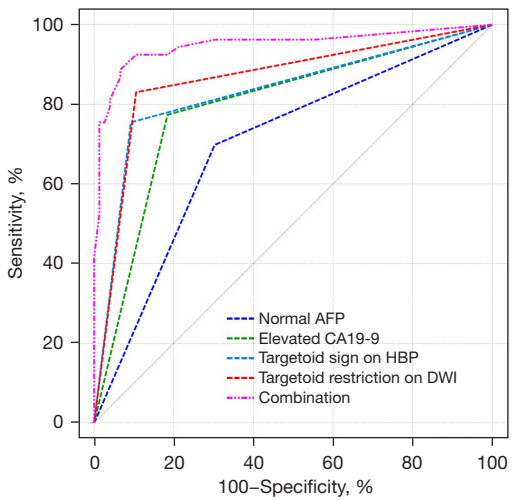

Figure 7 The ROC curve showed that the AUCs of normal AFP, elevated CA19-9, targetoid sign on HBP, targetoid restriction on DWI, and their combination in predicting mass-forming ICC were 0.698, 0.795, 0.831, 0.862, and 0.949, respectively. AFP, alpha fetoprotein; CA19-9, carbohydrate antigen 19-9; HBP, hepatobiliary phase; DWI, diffusion-weighted imaging; ROC, receiver operating characteristic; AUC, area under curve; ICC, intrahepatic cholangiocarcinoma.

It should be noted that targetoid sign refers to a target-like morphology that reflects peripheral hypercellularity and central fibrosis or ischemia within the tumor; hence, targetoid restriction on DWI correlates well with prominent central fibrosis. Since all ICCs contain a variable degree of fibrosis, the presence of fibrosis with accompanying edema might be responsible for the central hypointense area, whereas the peripheral tumor cells might contribute to the hyperintense zone of ICC on DWI (31,32). On the other hand, targetoid sign on HBP of mass-forming ICC is closely related to the dissemination of Gd-EOB-DTPA within the tumor. Fibrous stroma and intercellular matrix are present in the center to varying degrees, which may lead to retention and slow excretion of contrast agent within the tumor (19,33,34). Park *et al.* (27) reported that targetoid restriction on DWI is the most reliable imaging feature for distinguishing small mass-forming ICC from small HCC, indicating that DWI exhibits higher sensitivity in demonstrating the signal change derived from fibrosis than does T2WI and HBP for a mass-forming ICC with a diameter less than 3 cm. A similar result was found in our study with centrally fibrotic small ICC only showing targetoid restriction on DWI (*Figure 2E*). It is worth noting that scirrhous HCC (*Figure 5E,5F*) containing abundant fibrous stroma within the tumor can also have a targetoid appearance on DWI and/or HBP, which is difficult to differentiate from mass-forming ICC (24,28). Park *et al.* (35) found that a proportion of arterial hyperenhancement ≥20% of tumor diameter was only a remarkable feature in distinguishing scirrhous HCCs from mass-forming ICCs.

Table 5 Diagnostic performance of independent predictors and their combination for mass-forming ICC

Factors	AUC (95% CI)	Sensitivity (%)	Specificity (%)	Accuracy (%)	PPV (%)	NPV (%)
Normal AFP	0.698 (0.604, 0.791)	69.8	69.7	69.8	61.7	76.8
Elevated CA19-9	0.795 (0.712, 0.877)	77.4	81.6	79.8	74.5	83.8
Targetoid sign on HBP	0.831 (0.753, 0.910)	75.5	90.8	84.5	85.1	84.1
Targetoid restriction on DWI	0.862 (0.791, 0.934)	83.0	89.5	86.8	84.6	88.3
Combination	0.949 (0.905, 0.993)	88.7	93.4	91.5	90.4	88.8

ICC, intrahepatic cholangiocarcinoma; AUC, area under curve; CI, confidence interval; PPV, positive predictive value; NPV, negative predictive value; AFP, alpha fetoprotein; CA19-9, carbohydrate antigen 19-9; HBP, hepatobiliary phase; DWI, diffusion-weighted imaging.

As mentioned above, both fibrosis and central ischemia or necrosis can result in the targetoid appearance. Sarcomatous HCCs usually show a necrotic tendency and manifest as hypovascular tumors with rim enhancement due to the rapid growth of sarcomatous components composed of poorly differentiated cells (24).

Since our results demonstrated limited incremental value of targetoid appearance in discriminating mass-forming ICCs from other fibrosis-rich HCCs, we found that integrating CA19-9 into a diagnostic strategy can significantly help in differentiation. Previous studies have indicated that tumor biomarkers are critical to the treatment response and prognostic prediction of PLC. CA19-9 has been reported to be closely related to ICC, and the sensitivity and specificity of elevated CA19-9 in diagnosing ICC are 72% and 84%, respectively (36). The most commonly reported threshold value of CA19-9 is approximately 37 U/mL (37), which is the same as that in our study. We further found that 77.4% of patients with ICC had mild to moderate elevated CA19-9. Nonetheless, it should be noted that the utility of CA19-9 alone in discriminating remains unsatisfactory owing to the overlap with other malignant tumors. According to our result, a diagnostic regimen focused on imaging features, in particular targetoid appearance on DWI and/or HBP, combined with serum tumor markers (normal AFP and elevated CA 19-9), can improve the diagnostic performance of mass-forming ICCs.

There are several limitations in our study. First, we selected patients ICCs and those with atypical HCC and HBV infection, constituting an inherent selection bias. Second, there are no standard diagnostic criteria for atypical HCC, and thus selection bias might have been present in the enrollment of patients with atypical HCC, including those with scirrhous HCC, sarcomatous HCC, or hypovascular HCC. Third, our study did not include hypervascular mass-forming ICC with an atypical imaging pattern of nonperipheral arterial enhancement. Pathologically, hypervascular mass-forming ICC is a well-differentiated tumor with abundant tumor vasculature, a higher proportion of cellular area, and a less-central fibrosis. Occasionally, hypervascular ICCs do manifest a targetoid appearance on DWI and/or HBP. Finally, our study did not include other hepatic tumors that may demonstrate a targetoid appearance, especially cHCC-CCA, lymphoma, and metastasis. Clinically, it is important to differentiate ICC from atypical HCC as well as other mimicking tumors.

Conclusions

In conclusion, a diagnostic regimen integrating tumor markers (CA19-9, AFP) and imaging biomarkers (targetoid restriction on DWI and/or targetoid sign on the HBP) using Gd-EOB-DTPA-enhanced MRI could help to differentiate mass-forming ICCs from atypical HCCs and achieve high diagnostic performance for mass-forming ICCs in at-risk patients with HBV. This combination achieved a diagnostic specificity for mass-forming ICCs of more than 90%, and thus its application may reduce the need for biopsy.

Acknowledgments

Funding: The study was supported by the Natural Science Foundation of Henan Province (No. 232300421187) and the Medical Science Research Fund 2022 Research Project (No. YWJKJJHKYJJ-BXS5-22039).

Footnote

Conflicts of Interest: All authors have completed the ICMJE uniform disclosure form (available at https://qims.amegroups.com/article/view/10.21037/qims-23-396/coif). The authors have no conflicts of interest to declare.

Ethical Statement: The authors are accountable for all aspects of the work in ensuring that questions related to the accuracy or integrity of any part of the work are appropriately investigated and resolved. The study was conducted in accordance with the Declaration of Helsinki (as revised in 2013) and was approved by the Institutional Review Board of the First Affiliated Hospital of Henan University of Chinese Medicine (No. 2023HL-034-01). Written informed consent was waived due to the retrospective nature of the study.

References

1. Kanda T, Goto T, Hirotsu Y, Moriyama M, Omata M. Molecular Mechanisms Driving Progression of Liver Cirrhosis towards Hepatocellular Carcinoma in Chronic Hepatitis B and C Infections: A Review. Int J Mol Sci 2019;20:1358.
2. Massarweh NN, El-Serag HB. Epidemiology of Hepatocellular Carcinoma and Intrahepatic Cholangiocarcinoma. Cancer Control 2017;24:1073274817729245.
3. Ogasawara S, Koroki K, Kanzaki H, Kobayashi K, Kiyono S, Nakamura M, Kanogawa N, Saito T, Kondo T, Nakagawa R, Nakamoto S, Muroyama R, Chiba T, Kato N. Changes in therapeutic options for hepatocellular carcinoma in Asia. Liver Int 2022;42:2055-66.
4. Song Y, Cai M, Li Y, Liu S. The focus clinical research in intrahepatic cholangiocarcinoma. Eur J Med Res 2022;27:116.
5. Mejia JC, Pasko J. Primary Liver Cancers: Intrahepatic Cholangiocarcinoma and Hepatocellular Carcinoma. Surg Clin North Am 2020;100:535-49.
6. Santillan C, Chernyak V, Sirlin C. LI-RADS categories: concepts, definitions, and criteria. Abdom Radiol (NY) 2018;43:101-10.
7. Fowler KJ, Potretzke TA, Hope TA, Costa EA, Wilson SR. LI-RADS M (LR-M): definite or probable malignancy, not specific for hepatocellular carcinoma. Abdom Radiol (NY) 2018;43:149-57.
8. Jiang H, Song B, Qin Y, Chen J, Xiao D, Ha HI, Liu X, Oloruntoba-Sanders O, Erkanli A, Muir AJ, Bashir MR. Diagnosis of LI-RADS M lesions on gadoxetate-enhanced MRI: identifying cholangiocarcinoma-containing tumor with serum markers and imaging features. Eur Radiol 2021;31:3638-48.
9. Kierans AS, Makkar J, Guniganti P, Cornman-Homonoff J, Lee MJ, Pittman M, Askin G, Hecht EM. Validation of Liver Imaging Reporting and Data System 2017 (LI-RADS) Criteria for Imaging Diagnosis of Hepatocellular Carcinoma. J Magn Reson Imaging 2019;49:e205-15.
10. van der Pol CB, Lim CS, Sirlin CB, McGrath TA, Salameh JP, Bashir MR, Tang A, Singal AG, Costa AF, Fowler K, McInnes MDF. Accuracy of the Liver Imaging Reporting and Data System in Computed Tomography and Magnetic Resonance Image Analysis of Hepatocellular Carcinoma or Overall Malignancy-A Systematic Review. Gastroenterology 2019;156:976-86.
11. Lee SM, Lee JM, Ahn SJ, Kang HJ, Yang HK, Yoon JH. LI-RADS Version 2017 versus Version 2018: Diagnosis of Hepatocellular Carcinoma on Gadoxetate Disodium-enhanced MRI. Radiology 2019;292:655-63.
12. Chong YS, Kim YK, Lee MW, Kim SH, Lee WJ, Rhim HC, Lee SJ. Differentiating mass-forming intrahepatic cholangiocarcinoma from atypical hepatocellular carcinoma using gadoxetic acid-enhanced MRI. Clin Radiol 2012;67:766-73.
13. Tsuchiya N, Sawada Y, Endo I, Saito K, Uemura Y, Nakatsura T. Biomarkers for the early diagnosis of hepatocellular carcinoma. World J Gastroenterol 2015;21:10573-83.
14. Wáng YXJ, Wang X, Wu P, Wang Y, Chen W, Chen H, Li J. Topics on quantitative liver magnetic resonance imaging. Quant Imaging Med Surg 2019;9:1840-90.
15. Zhou J, Sun H, Wang Z, Cong W, Wang J, Zeng M, et al. Guidelines for the Diagnosis and Treatment of Hepatocellular Carcinoma (2019 Edition). Liver Cancer 2020;9:682-720.
16. Vietti Violi N, Lewis S, Hectors S, Said D, Taouli B. Radiological Diagnosis and Characterization of HCC. 2019.
17. Lendvai G, Szekerczés T, Illyés I, Dóra R, Kontsek E, Gógl A, Kiss A, Werling K, Kovalszky I, Schaff Z, Borka K. Cholangiocarcinoma: Classification, Histopathology and Molecular Carcinogenesis. Pathol Oncol Res 2020;26:3-15.
18. Jang JK, Choi SH, Byun JH, Park SY, Lee SJ, Kim SY, Won HJ, Shin YM, Kim PN. New strategy for Liver Imaging Reporting and Data System category M to improve diagnostic performance of MRI for hepatocellular carcinoma ≤ 3.0 cm. Abdom Radiol (NY) 2022;47:2289-98.
19. Chernyak V, Fowler KJ, Kamaya A, Kielar AZ, Elsayes KM, Bashir MR, Kono Y, Do RK, Mitchell DG, Singal AG, Tang A, Sirlin CB. Liver Imaging Reporting and Data System (LI-RADS) Version 2018: Imaging of Hepatocellular Carcinoma in At-Risk Patients. Radiology 2018;289:816-30.
20. Elmohr M, Elsayes KM, Chernyak V. LI-RADS: Review and updates. Clin Liver Dis (Hoboken) 2021;17:108-12.
21. Flores JE, Thompson AJ, Ryan M, Howell J. The Global Impact of Hepatitis B Vaccination on Hepatocellular Carcinoma. Vaccines (Basel) 2022.
22. Zhu RX, Seto WK, Lai CL, Yuen MF. Epidemiology of Hepatocellular Carcinoma in the Asia-Pacific Region. Gut Liver 2016;10:332-9.
23. Kovac JD, Ivanovic A, Milovanovic T, Micev M, Alessandrino F, Gore RM. An overview of hepatocellular carcinoma with atypical enhancement pattern: spectrum

of magnetic resonance imaging findings with pathologic correlation. Radiol Oncol 2021;55:130-43.
24. Kim JH, Joo I, Lee JM. Atypical Appearance of Hepatocellular Carcinoma and Its Mimickers: How to Solve Challenging Cases Using Gadoxetic Acid-Enhanced Liver Magnetic Resonance Imaging. Korean J Radiol 2019;20:1019-41.
25. Hwang J, Kim YK, Min JH, Choi SY, Jeong WK, Hong SS, Kim HJ, Ahn S, Ahn HS. Capsule, septum, and T2 hyperintense foci for differentiation between large hepatocellular carcinoma (≥5 cm) and intrahepatic cholangiocarcinoma on gadoxetic acid MRI. Eur Radiol 2017;27:4581-90.
26. Granata V, Grassi R, Fusco R, Setola SV, Belli A, Ottaiano A, Nasti G, La Porta M, Danti G, Cappabianca S, Cutolo C, Petrillo A, Izzo F. Intrahepatic cholangiocarcinoma and its differential diagnosis at MRI: how radiologist should assess MR features. Radiol Med 2021;126:1584-600.
27. Park HJ, Kim YK, Park MJ, Lee WJ. Small intrahepatic mass-forming cholangiocarcinoma: target sign on diffusion-weighted imaging for differentiation from hepatocellular carcinoma. Abdom Imaging 2013;38:793-801.
28. Kovac JD, Milovanovic T, Dugalic V, Dumic I. Pearls and pitfalls in magnetic resonance imaging of hepatocellular carcinoma. World J Gastroenterol 2020;26:2012-29.
29. Min JH, Kim YK, Choi SY, Jeong WK, Lee WJ, Ha SY, Ahn S, Ahn HS. Differentiation between cholangiocarcinoma and hepatocellular carcinoma with target sign on diffusion-weighted imaging and hepatobiliary phase gadoxetic acid-enhanced MR imaging: Classification tree analysis applying capsule and septum. Eur J Radiol 2017;92:1-10.
30. Choi SY, Kim YK, Min JH, Kang TW, Jeong WK, Ahn S, Won H. Added value of ancillary imaging features for differentiating scirrhous hepatocellular carcinoma from intrahepatic cholangiocarcinoma on gadoxetic acid-enhanced MR imaging. Eur Radiol 2018;28:2549-60.
31. Jhaveri KS, Hosseini-Nik H. MRI of cholangiocarcinoma. J Magn Reson Imaging 2015;42:1165-79.
32. Lewis S, Besa C, Wagner M, Jhaveri K, Kihira S, Zhu H, Sadoughi N, Fischer S, Srivastava A, Yee E, Mortele K, Babb J, Thung S, Taouli B. Prediction of the histopathologic findings of intrahepatic cholangiocarcinoma: qualitative and quantitative assessment of diffusion-weighted imaging. Eur Radiol 2018;28:2047-57.
33. Inchingolo R, Maino C, Gatti M, Tricarico E, Nardella M, Grazioli L, Sironi S, Ippolito D, Faletti R. Gadoxetic acid magnetic-enhanced resonance imaging in the diagnosis of cholangiocarcinoma. World J Gastroenterol 2020;26:4261-71.
34. Mori H, Akimoto S. Liver-spleen contrast standardization of gadolinium-ethoxybenzyl-diethylenetriamine penta-acetic acid-enhanced magnetic resonance imaging based on cross-calibration. Quant Imaging Med Surg 2022;12:5343-57.
35. Park MJ, Kim YK, Park HJ, Hwang J, Lee WJ. Scirrhous hepatocellular carcinoma on gadoxetic acid-enhanced magnetic resonance imaging and diffusion-weighted imaging: emphasis on the differentiation of intrahepatic cholangiocarcinoma. J Comput Assist Tomogr 2013;37:872-81.
36. Macias RIR, Kornek M, Rodrigues PM, Paiva NA, Castro RE, Urban S, Pereira SP, Cadamuro M, Rupp C, Loosen SH, Luedde T, Banales JM. Diagnostic and prognostic biomarkers in cholangiocarcinoma. Liver Int 2019;39 Suppl 1:108-22.
37. Izquierdo-Sanchez L, Lamarca A, La Casta A, Buettner S, Utpatel K, Klümpen HJ, et al. Cholangiocarcinoma landscape in Europe: Diagnostic, prognostic and therapeutic insights from the ENSCCA Registry. J Hepatol 2022;76:1109-21.

Cite this article as: Han D, Li Y, He X, Zhang J, Zhou Y, Zhang J, Zhang L. Differentiating mass-forming intrahepatic cholangiocarcinoma from atypical hepatocellular carcinoma using Gd-EOB-DTPA-enhanced magnetic resonance imaging combined with serum markers in at-risk patients with hepatitis B virus. Quant Imaging Med Surg 2023;13(10):7156-7169. doi: 10.21037/qims-23-396

